Multi-tracer extension of the halo model

MNRAS **000**, 1–16 (2020) Preprint 1 July 2020 Compiled using MNRAS LATEX style file v3.0

Multi-tracer extension of the halo model: probing quenching and conformity in eBOSS

Shadab Alam,[1]★ John A. Peacock,[1] Katarina Kraljic,[1] Ashley J. Ross,[2] and Johan Comparat[3]

[1] *Institute for Astronomy, University of Edinburgh, Royal Observatory, Blackford Hill, Edinburgh, EH9 3HJ , UK*
[2] *Center for Cosmology and AstroParticle Physics, The Ohio State University, 191 West Woodruff Avenue, Columbus, Ohio 43210, USA*
[3] *Max-Planck-Institut für extraterrestrische Physik (MPE), Giessenbachstrasse 1, D-85748 Garching bei München, Germany*

1 July 2020

ABSTRACT

We develop a new Multi-Tracer Halo Occupation Distribution (MTHOD) framework for the galaxy distribution and apply it to the extended Baryon Oscillation Spectroscopic Survey (eBOSS) final data between $z = 0.7 - 1.1$. We obtain a best fit MTHOD for each tracer and describe the host halo properties of these galaxies. The mean halo masses for LRGs, ELGs and QSOs are found to be $1.9 \times 10^{13}\, h^{-1} M_\odot$, $1.1 \times 10^{12}\, h^{-1} M_\odot$ and $5 \times 10^{12}\, h^{-1} M_\odot$ respectively in the eBOSS data. We use the MTHOD framework to create mock galaxy catalogues and predict auto- and cross-correlation functions for all the tracers. Comparing these results with data, we investigate galactic conformity, the phenomenon whereby the properties of neighbouring galaxies are mutually correlated in a manner that is not captured by the basic halo model. We detect *1-halo* conformity at more than 3σ statistical significance, while obtaining upper limits on *2-halo* conformity. We also look at the environmental dependence of the galaxy quenching efficiency and find that halo mass driven quenching successfully explains the behaviour in high density regions, but it fails to describe the quenching efficiency in low density regions. In particular, we show that the quenching efficiency in low density filaments is higher in the observed data, as compared to the prediction of the MTHOD with halo mass driven quenching. The mock galaxy catalogue constructed in this paper is publicly available on this website†.

Key words: cosmology: large-scale structure of Universe – cosmology: dark matter – galaxies: formation – galaxies: haloes – galaxies: evolution

1 INTRODUCTION

Galaxies are fundamental building blocks of the Universe, and their large-scale spatial distribution is an important source of cosmological information. However, a full understanding of the formation of these objects within the cosmic web of large-scale structure is challenging, owing to the number of astrophysical processes that must be modelled and the wide dynamic range of scales on which these operate. In principle the dark matter distribution should give a direct and precise answer to where galaxies should form, given that the dominant physical process is gravitational collapse of matter. Therefore, one can attempt to predict the locations of galaxies in the Universe purely by studying dark matter dynamics, which is a much simpler task in the ΛCDM model than performing calculations that include full baryonic physics.

This approach has led to the widely-used halo model (HOD: Seljak 2000; Peacock & Smith 2000; Benson et al. 2000; White et al. 2001; Berlind & Weinberg 2002; Cooray & Sheth 2002), which establishes the connection between dark matter haloes and galaxies. It has been highly successful for magnitude limited sample of bright galaxies in past galaxy redshift surveys (e.g. Eisenstein et al. 2011; Liske et al. 2015). The current generation of surveys (e.g. eBOSS: Dawson et al. 2016) and forthcoming surveys (e.g. DESI: DESI Collaboration et al. 2016) are in contrast targeting deeper samples and in particular selecting galaxies with special photometric properties. This brings a new challenge in terms of understanding the special locations that these galaxies might inhabit within the dark matter distribution, so that we can use them as tracers in order to obtain unbiased cosmological constraints. But this also offers a great opportunity in using these galaxies to understand certain aspects of galaxy formation physics, and to enhance cosmological constraints by exploiting information contained in the cross-correlations between the different populations. This goal requires the development of methods that not only

† https://www.roe.ac.uk/~salam/MTHOD/
★ E-mail: salam@roe.ac.uk

predict the locations of galaxies within the population of dark matter haloes, but which can also map their photometric properties. There have been several attempts in the past to extend the halo model in order to predict the photometric properties of galaxies (e.g. Scranton 2002; Cooray 2006; Skibba & Sheth 2009; Xu et al. 2018).

Galaxies exhibit a wide range of properties with rather diverse behaviours. The colour distribution of galaxies shows bi-modal behaviour representing largely red and blue population (e.g. Strateva et al. 2001; Baldry et al. 2004; Balogh et al. 2004). More massive galaxies mostly tend to be red spheroids, while less massive galaxies tend to be star-forming discs (e.g. Kauffmann et al. 2003). For the purpose of cosmological surveys, one can conveniently think about three kinds of galaxies as follows:

- Quenched galaxies: The sub-population of galaxies with effectively no active star formation. Such galaxies appear red in colour and are generally massive and old. They generally live at the centres of massive haloes or in high density regions. There are several processes thought to be responsible for 'quenching', i.e. the cessation of star formation (e.g. cold gas stripping, harassment, strangulation or starvation). Galaxy redshift surveys such as eBOSS and DESI typically select a specific sub-sample of quenched galaxies, known as Luminous Red Galaxies (LRG), based on photometric observations (see Section 2.1 for the details of eBOSS LRG selection).
- Star-forming galaxies: The sub-population of galaxies with active star formation. Such galaxies typically appear blue and generally avoid high densities or the centres of the most massive haloes. They are also expected to be predominantly low mass galaxies. The complex interplay between density and tidal environment makes it more difficult to predict the locations of such galaxies. eBOSS and DESI target a very specific sub-sample of star forming galaxies with high emission in OII 3727Å line flux – Emission Line galaxies (ELG; see Section 2.2 for the details of eBOSS ELG selection).
- AGN: Galaxies with strong emission from their central black hole region known as Active Galactic Nuclei (AGN). The importance of environment and baryonic processes during their formation makes the ability to predict their location within dark matter distribution challenging. eBOSS and DESI target a specific subset of such AGN that are especially bright in the optical bands, also known as Quasi Stellar Objects (QSOs; see Section 2.3 for the details of eBOSS QSO selection).

The current and future surveys of these three types of galaxies have great potential to measure whether these different kinds of galaxies have any special clustering properties, and thus to give insights into the physical processes involved in their formation. At the same time, more complicated formation mechanisms introduce astrophysical systematics in the clustering properties of these galaxies, which need to be accounted for in order to infer unbiased cosmological parameters. The halo model assumes that halo mass can predict the location of different kinds of galaxies within the dark matter field. One can argue that non-linear evolution of both dark matter and baryons can add additional features in the relation between dark matter and galaxies. For example large-scale tidal fields can affect the accretion rate of haloes (Musso et al. 2018), with smaller haloes around filaments possibly growing more slowly (Hahn et al. 2009; Castorina et al. 2016; Borzyszkowski et al. 2017). In theoretical models, galaxy quenching is assumed to be driven mainly by halo mass (e.g. Dekel & Birnboim 2006; Cattaneo et al. 2006; Correa et al. 2018); this concept is successful in describing galaxy clustering and weak gravitational lensing (Zu & Mandelbaum 2016). In principle, for galaxy evolution, the cosmic web can also play a significant role by directing cold gas flows along filaments (Kereš et al. 2005), thus providing material for star formation to galaxies along filaments leading to suppression of quenching (Kleiner et al. 2017). It is also important to note that the central black holes in galaxies grow with galaxies. Therefore, a massive black hole can initiate feedback which can regulate the gas causing quenching. Such process can have impact on galaxy properties beyond halo mass.

In this paper we develop a halo model called Multi-Tracer Halo Occupation Distribution (`MTHOD` hereafter), which extends the standard HOD to include the simultaneous treatment of multiple kinds of galaxies. The general statistical framework we present is extremely useful in practical modelling of current and future surveys. This will allow us to interpret cross-correlation measurements and test the halo model in ways not possible with a single-tracer model. We apply the `MTHOD` framework to eBOSS data and show its potential. In principle the vanilla version of the model contains minimal astrophysical information on galaxy clustering. Our approach is always to work with the simplest ansatz unless it fails through the data showing a signature of additional physics. We test this model by making detailed comparison with data and show that the fiducial model indeed fails to reproduce observations exactly. We then develop a possible extension of the fiducial model and highlight the insight this gives us regarding galaxy formation physics. We do not perform cosmological parameter analysis here; this will be addressed in future studies.

In particular, we focus on galactic conformity, which is a phenomenon whereby the properties of neighbouring galaxies are mutually correlated in a manner that is not captured by the basic halo model. Depending on the spatial scale considered, two regimes can be distinguished: the so-called *1-halo* conformity, when the neighbouring galaxies belong to the same halo, and *2-halo* conformity, extending to scales beyond the virial radius of haloes. Galactic conformity was first identified by Weinmann et al. (2006) as an intriguing correlation between the star-formation properties of central galaxies and those of their satellites, with the fraction of red, passive satellites around a red, passive central being significantly higher than around a blue, active central. Since then, this *1-halo* conformity has been confirmed by several authors both in the local Universe (e.g. Kauffmann et al. 2010; Wang & White 2012; Kauffmann et al. 2013; Robotham et al. 2013; Phillips et al. 2014; Knobel et al. 2015; Treyer et al. 2018) and at higher redshifts (Hartley et al. 2015; Kawinwanichakij et al. 2016; Berti et al. 2017). A galactic conformity type signal was also reported in Ross & Brunner (2009) which used halo model and required early and late type galaxies to be in different halos. Beyond this, a detection of *2-halo* conformity was reported by Kauffmann et al. (2013); however, this result is still debated as possibly driven by selection bias (Sin et al. 2017; Lacerna et al.

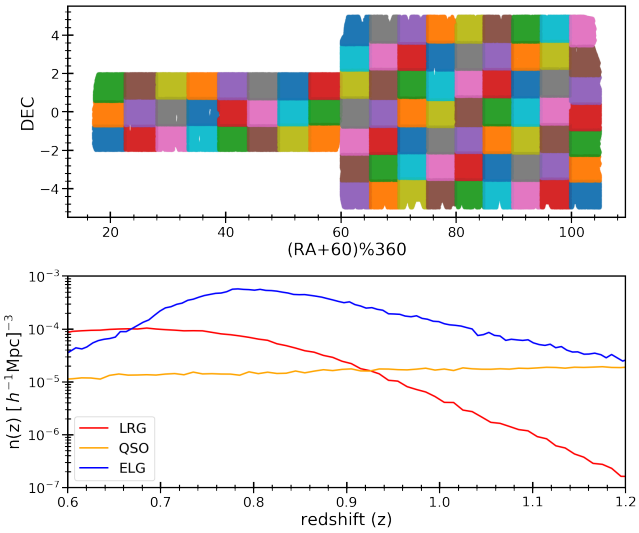

Figure 1. The sky coverage and number density distribution of our sample used in this paper. The top panel shows the sky coverage of the sub-sample of eBOSS data with different colours representing the jackknife realisations. The bottom panel shows the number density distribution of each tracer in the sample.

2018; Tinker et al. 2018). Interestingly Calderon et al. (2018) reported no signature of *1-halo* but a robust detection of *2-halo* galactic conformity at low redshift in SDSS DR7 data. Galactic conformity is usually identified in observations by first identifying central and satellite galaxies that are prone to systematic errors. Our method avoids the need for such identification and works at the population level to constrain this effect.

The paper is organised as follows. First, we introduce the details of the `MTHOD` model in Section 2, then we describe the eBOSS data used in Section 3, followed by the description of the measurement and systematics in Section 4. We describe the details of the analysis in Section 5 and present the results of applying `MTHOD` in Section 6. We finish by summarising our results with discussion of their implication in Section 7.

2 DATA

We are using data obtained by the extended Baryon Oscillation Spectroscopic (eBOSS) survey (Dawson et al. 2013). The eBOSS project is one of the programmes within the wider 5-year Sloan Digital Sky Survey-IV (SDSS-IV Blanton et al. 2017) using the 2.5m Sloan Telescope (Gunn et al. 2006) and BOSS spectrograph (Smee et al. 2013). The eBOSS sample consists of four different types of tracers, namely Luminous Red Galaxies (LRG); Emission Line Galaxies (ELG); Quasi-Stellar Objects (QSO); and Lyman Alpha Forest. We are using a subset of the eBOSS samples that covers the redshift range from 0.7 to 1.1, where all of the three tracers of interest, namely LRG, ELG and QSOs, overlap. The overlap region can be used to study these tracers with cross-correlations and this results in dense enough galaxy samples to probe the underlying dark matter distribution through the combined samples. We use intermediate versions of the data release 16 (DR16) catalogues produced by the eBOSS collaboration (eBOSS collaboration in prep.; Raichoor et al. in prep). Any changes between the version we have used and the final versions are expected to be minor and mainly affect the results at large scales. We now briefly describe the relevant aspects of eBOSS sample selection.

2.1 LRG selection

The LRGs are expected to be the brightest and reddest galaxies living in massive dark matter haloes, and hence they have a high bias parameter. The eBOSS LRGs are selected from SDSS imaging data (Gunn et al. 2006; Abazajian et al. 2009) in combination with infrared photometry from WISE (Wright et al. 2010; Lang et al. 2014) using the following target selection rules:

$$r - i > 0.98, \quad (1)$$

$$r - W1 > 2(r - i), \quad (2)$$

$$i - z > 0.625, \quad (3)$$

where r, i and z are the model magnitudes of SDSS photometric bands and $W1$ refers to the WISE photometry in the 3.4 micron channel. The selections in equations 1, 2 and 3 allow us to pick out the desired redshift range, to reduce stellar contamination and to reduce interlopers from below redshift 0.6 respectively. The details of how these rules were derived and additional considerations are discussed in Prakash et al. (2015, 2016).

2.2 ELG selection

The ELGs are selected based on high OII flux and are expected to be star forming galaxies that are typical of the population at high redshift. An earlier study about ELG selection with SDSS infrastructure was performed by Comparat et al. (2013a,b) and a pilot survey of ELGs testing different target selection algorithms is reported in Comparat et al. (2016). The ELG sample in eBOSS is selected from the DECAM Legacy survey (DECaLS: Dey et al. 2019). The target selection rules for ELGs in the North Galactic Cap (NGC) and South Galactic Cap (SGC) are slightly different due to the availability of deeper data in the SGC. We use only the SGC region of the ELG sample for cross-correlations studies due to the overlap with other tracers, hence we summarise only the SGC selection here. The ELG selection has two parts, the first of which is to select star forming galaxies corresponding to the OII emission using the following criterion:

$$21.825 < g < 22.825. \quad (4)$$

The second rule for ELG selection is given by the following criteria, which preferentially select galaxies around redshift 1.0:

$$-0.068(r - z) + 0.457 < g - r < 0.112(r - z) + 0.773, \quad (5)$$

$$0.218(g - r) + 0.571 < r - z < -0.555(g - r) + 1.901, \quad (6)$$

where g, r, z are the observed magnitudes in the DECaLS g, r and z photo-metric bands. More details of how these rules were derived and additional considerations are discussed in Raichoor et al. (2017).

2.3 QSO selection

The density requirements of the other targets in the eBOSS sample restrict the density of the eBOSS QSO sample. Myers et al. (2015) describe in detail all the requirements and how the QSO sample is selected. First a super-sample of QSOs is selected from the SDSS imaging with either $g < 22$ or $r < 22$ and $i_f > 17$, where g and r are the psf magnitudes of the SDSS photometric bands and i_f is the FIBER2MAG. This super-sample is passed through the XDQSOz algorithm (Bovy et al. 2012), which assigns a probability for each object being a QSO in a given redshift range using the photometric flux in $ugriz$. The eBOSS sample uses a probabilistic cut of $P_{\rm QSO}(z > 0.9) > 0.2$. There is also an infrared cut used to remove stellar contamination with $m_{\rm opt} - m_{\rm WISE} \geq (g-i)+3$, where $m_{\rm opt}$ and $m_{\rm WISE}$ are the optical and WISE magnitudes respectively given by equations 1 and 2 in Myers et al. (2015).

We show the sky coverage of the eBOSS sub-sample, where all three tracers are observed, in the top panel of Figure 1. The number density distribution of the three tracers used in this paper are shown in the bottom panel of Figure 1. We note that around redshift 0.86 the number density of LRG, ELG and QSO are 10^{-4}, 4×10^{-4} and $2 \times 10^{-5} \left[h^{-1}{\rm Mpc} \right]^{-3}$, respectively. The redshift cut between 0.7 and 1.1 is chosen to have ELG number density above $10^{-4} \left[h^{-1}{\rm Mpc} \right]^{-3}$. The LRG number density drops sharply above redshift 0.9, this means that the cross-correlation signal of LRG is dominated by galaxies at lower redshift. We have looked at results by applying redshift cut between 0.7 and 0.9 and found the results are consistent with our fiducial redshift cut.

2.4 Random catalogues and systematic weights

Each of the large scale structure catalogues requires a corresponding random catalogue representing the sampling of the volume by the tracer. This is important to account for effects of survey geometry, survey mask, observational conditions, instrument efficiency etc. over the period of the full survey. The details of how these random catalogues are generated is described in Ross et al. (2020) for LRGs & QSOs and Raichoor et al. (2020) for the ELG sample. The photometric galaxy sample on which target selection is applied for tracers shows correlation with various galactic maps such as stellar density, extinction coefficient, airmass, seeing and depth in photometric observations. The correlation of target density with such systematic maps is derived and corrected using weights described in Ross et al. (2020) and Raichoor et al. (2020).

3 MULTI-TRACER HOD (MTHOD)

We develop a generalised Halo Occupation Distribution model describing populations of multiple tracers. The model assumes that all galaxies form and reside within dark matter haloes, with properties dictated primarily by the mass of the host halo. We further make the common assumption that any dark matter halo can have two types of galaxies – central and satellite. We describe the detailed model formulation for central and satellite galaxies below.

3.1 Central galaxies

The fiducial model assumes that the probability of having a central galaxy of a given type is a function of halo mass only. The total probability for a halo to host a central galaxy is given by the summed probabilities of a central galaxy over all the tracers and is written as follows:

$$p^{\rm tot}_{\rm cen}(M_{\rm h}) = \sum_{tr \epsilon TR} p^{\rm tr}_{\rm cen}(M_{\rm h}), \tag{7}$$

where the sum goes over all tracers in the list $TR = \{{\rm LRG}, {\rm QSO}, {\rm ELG}\}$. This equation requires a constraint of $p^{\rm tot}_{\rm cen} \leq 1$ for any halo mass. This also assumes that the central galaxy probabilities of different types of tracers are independent of each other. This is a major assumption of the fiducial model and will be discussed further in the later sections.

The LRG sample is assumed to inhabit largely massive haloes and effectively $p^{\rm LRG}_{\rm cen}$ has been modelled successfully with a error function given in equation 8 which is essentially saying that the LRG sample central galaxy has a cut-off halo mass ($M_{\rm c}$) and a dispersion (σ_M) in mass-to-light ratio:

$$p^{\rm LRG}_{\rm cen} = \langle N_{\rm erf}(M_{\rm h}) \rangle = \frac{1}{2} p_{\rm max} \, {\rm erfc} \left(\frac{\log_{10} M_{\rm c} - \log_{10} M_{\rm h}}{\sqrt{2} \log_{10}(e) \sigma_M} \right). \tag{8}$$

Where the parameter $p_{\rm max}$ controls the saturation level of the occupation probability and has been set to unity in the past, implying that the most massive haloes are guaranteed to possess a central galaxy. Alternatively, Halo Abundance Matching (HAM) has also been used to model clustering of LRGs (Favole et al. 2016). The statistics of central QSOs are harder to parameterize due to the intrinsic complications of AGN physics and also practical issues of the optical selection function. In the past, QSO central galaxies have been modelled using an error function model (e.g. Richardson et al. 2012), but this is one of the major uncertainties regarding the halo mass distribution of optically selected QSOs. For example, one can argue that LRGs have massive black holes and hence could host all QSOs with some duty cycle for black hole activity. Because the number of QSOs is very small compared to other classes of galaxies and for the lack of any clearly preferred alternative, we adopt the error function form given in equation 8 to model the central galaxy probability for QSOs. We will later discuss the implications of this assumption. How one can learn about AGN physics by comparing different choices concerning central galaxy occupation for QSOs will be studied in a follow-up paper (Alam et al. in prep.). For a semi-analytic approach to model AGN see Georgakakis et al. (2019).

Emission line galaxies (ELGs) emit strongly in OII 3737Å, caused by active star formation. Such star formation processes are inefficient at the centres of massive haloes, reflecting the absence of cold gas. This suggests that an error function model for ELG central galaxies may not be realistic. Comparat et al. (2015) suggested a semi-analytic model of galaxy formation based on the study of luminosity function of OII bright galaxies. Gonzalez-Perez et al. (2018) have used this model to study ELGs and suggested that the central probability of ELGs should be reduced for high mass haloes as shown in their Figure 9. Therefore, we propose the HMQ (High Mass Quenched) model for the central proba-

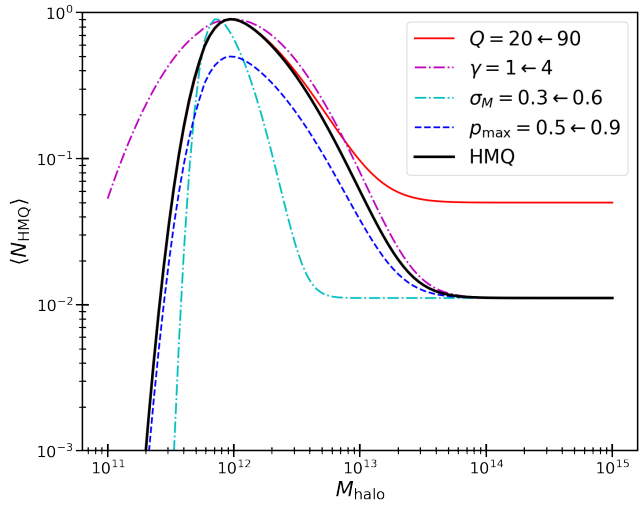

Figure 2. ELG occupation probability for the Halo mass quenching model with an illustration of the effect of individual parameters. The black solid line shows fiducial model. The red solid, magenta dashed-dotted, cyan dashed-dotted and blue dashed lines show the impact of the parameters Q, γ, σ_M and $p_{\rm max}$ respectively, when changed from the fiducial values. The legend also displays the values of parameters used in this illustration.

bility of ELGs with a skewed Gaussian function, as follows:

$$\left\langle N_{\rm HMQ}(M_{\rm h}) \right\rangle = 2A\phi(M_{\rm h})\Phi(\gamma M_{\rm h}) + \frac{1}{2Q}\left[1 + {\rm erf}\left(\frac{\log_{10} M_h - \log_{10} M_c}{0.01}\right)\right], \quad (9)$$

$$\phi(x) = \mathcal{N}(\log_{10} M_c, \sigma_M), \quad (10)$$

$$\Phi(x) = \int_{-\infty}^{x} \phi(t)\, dt = \frac{1}{2}\left[1 + {\rm erf}\left(\frac{x}{\sqrt{2}}\right)\right], \quad (11)$$

$$A = \frac{p_{\rm max} - 1/Q}{\max(2\phi(x)\Phi(\gamma x))}. \quad (12)$$

The effect of various parameters on the HMQ occupation function is illustrated in Figure 2. The black line shows the fiducial model and each coloured line illustrates the impact of one parameter with details in the legend. The parameter M_c is the cut-off mass of ELG centrals impacting the location of the peak in occupation probability and not shown in Figure 2 to avoid clutter. Q sets the quenching efficiency for high mass haloes; a larger value of Q implies more efficient quenching as shown with a red solid line. The function $\phi(M_h)$ is the normal distribution given in equation 10 and $\Phi(M_h)$ is the cumulative density function of $\phi(M_h)$ given in equation 11. These two functions depend on the parameters γ controlling the skewness as shown by magenta dashed-dotted line and σ_M controlling the width illustrated with cyan dashed-dotted line. The parameter A sets the overall formation efficiency of ELGs given in equation 12 and depends on $p_{\rm max}$, which is illustrated with blue dashed line. We will also consider a more standard error function model for ELG central galaxy probabilities in order to compare the differences between the two cases. Note that the error function model for ELG central is non-physical and included only for the purpose of comparison.

Once we define the occupation recipe for central galaxies, we need to assign their positions and velocities so that the redshift-space clustering can be compared with data. The central galaxies in the fiducial model are placed at the centre of the dark matter haloes and the velocities given to them are the halo core velocities which are computed using the particles within 10% of the virial radius of the centre of the halo. In principle, one could imagine that the central galaxy could either deviate from the centre of the halo or have velocity bias. Such variations will be considered in the future (Alam et al. in prep.) as the current data do not allow such an extra freedom to be constrained. Note that these assumptions do not affect the qualitative nature of the results presented in this paper.

3.2 Satellite galaxies

The satellite galaxies in the dark matter haloes are expected to inhabit subhaloes. But resolving all the subhaloes is highly demanding in terms of simulation resolution; therefore we will model satellite galaxies following the dark matter distribution with little additional freedom. We first assume that the number of satellite galaxies obeys Poisson statistics. Current limited data sets do not allow us to test this assumption, but it will be possible with future surveys. We assume that the mean number of satellite galaxies depends only on the halo mass and is independent of presence of satellites or centrals of other types of galaxies in the neighbourhood. In the scenario when the cosmic web influences satellites formation of a given type, one would expect both of these assumptions of the fiducial model to be invalid. We will test if data requires these assumptions to be changed by looking at cross-correlations. In principle, a more complex model for the satellite galaxies can be motivated based on current understanding of galaxy formation and results from various hydrodynamical simulations. But initially we will stay with this simple model; if it fails to describe the observed data, then that will be evidence that a more complicated satellite population model is needed. The mean number of satellite galaxies as a function of halo mass is given by the following equation:

$$\left\langle N^{\rm tot}_{\rm sat} \right\rangle (M_{\rm halo}) = \sum_{tr \epsilon TR} \left\langle N^{\rm tr}_{\rm sat} \right\rangle (M_{\rm halo}), \quad (13)$$

where the sum is over all different tracers in the sample. The number of satellite galaxies per halo is given by following functional form:

$$\langle N_{\rm sat} \rangle (M_{\rm halo}) = \left(\frac{M_{\rm h} - \kappa M_c}{M_1}\right)^{\alpha}. \quad (14)$$

The number of satellite galaxies is essentially assumed to be a power law with index α and characteristic satellite mass M_1. The parameter κ sets a cut-off mass in units of M_c below which the probability of a satellite galaxy is zero. We use the same functional form to model the number of satellites for all three tracers in the sample, with independent parameters in each case. We do however require the existence of a central galaxy in a halo before it is allowed to host any LRG satellite, following Zheng et al. (2005) and Guo et al. (2015). But this assumption does not affect our results because LRG satellites inhabit massive halos with a central occupation probability of unity. The ELG and QSO satellite galaxies can be hosted by haloes without any central galaxy, although this rarely happens in practice. We also set $\kappa = 1$ when

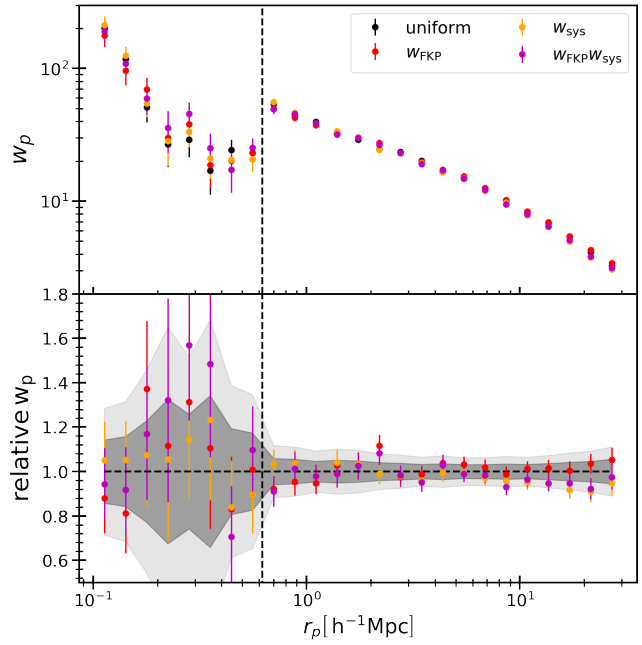

Figure 3. The projected correlation function for ELGs, using different systematic weights. This plot shows that the effect of the systematic weight is negligible in the w_p measurements between scales of 1–30 h^{-1}Mpc. Therefore our results should be insensitive to the details of systematic weights of different samples. The black-dashed vertical line shows the fibre-collision scale for eBOSS at the mean redshift of 0.86.

ELG satellites are modelled with the HMQ model based on the results from Gonzalez-Perez et al. (2018). One could also imagine introducing correlations between satellites and centrals of different tracers. We will consider some aspects of such correlations later as an extension of the fiducial model.

The satellite galaxies are distributed following an NFW density profile for the haloes, where the concentration for each halo is measured in the N-body simulation (see Section 5). We also assign isotropic random velocities to satellites with the same velocity dispersion as the dark matter. Due to the lack of small-scale clustering in the current data, the results in this paper are insensitive to such choices and the data are not sufficient to inform us whether these assumptions need to be modified.

Our approach is to use the simplest model unless observational data demand additional extension. Note that in our formalism we populate all galaxies simultaneously, so that it naturally avoids the non-physical situation of having central galaxies of different tracers in the same halo at the same time. One of the ways we will test the validity of various assumptions is by looking at the cross-correlations between different tracers.

4 MEASUREMENTS AND SYSTEMATICS

We first estimate the position of each galaxy in 3-dimensional space by converting redshift to the line-of-sight distance using the fiducial cosmology ($\Omega_m = 0.307$, $h = 0.67$). We then measure galaxy auto-correlation functions using the minimum variance Landay-Szalay estimator (Landy & Szalay 1993) given by:

$$\xi_{\rm auto}(\vec{r}) = \frac{DD(\vec{r}) - 2DR(\vec{r}) + RR(\vec{r})}{RR(\vec{r})}, \quad (15)$$

where DD, DR and RR are numbers of galaxy-galaxy, galaxy-random and random-random pairs as a function of vector offset in 3-dimensional space. The cross-correlations are measured using following estimator:

$$\xi_{\rm cross}(\vec{r}) = \frac{D_1D_2(\vec{r})}{D_1R_2(\vec{r})} - 1, \quad (16)$$

where D_1D_2 and D_1R_2 are numbers of galaxy-galaxy counts and galaxy-random counts. We note that redshift-space distortions make the line-of-sight a special direction, and therefore we project the 3-dimensional space onto a 2-dimensional space that decomposes pair separation vectors along the line-of-sight ($s_\parallel$) and perpendicular to the line-of-sight ($s_\perp$). This gives us the 2-dimensional correlation function $\xi(s_\parallel, s_\perp)$. We then measure the projected correlation function (w_p) by integrating the 2-dimensional correlation function along the line-of-sight between $s_\parallel = -40\,h^{-1}$Mpc to $s_\parallel = +40\,h^{-1}$Mpc and using 25 logarithmic bins in $s_\perp$ between $0.1\,h^{-1}$Mpc and $30\,h^{-1}$Mpc. The projected correlation function helps us constrain the HOD parameters that govern the galaxy-halo connection. We create 86 jackknife regions for our sample and estimate jackknife covariances wherever needed in this analysis.

The clustering measurement is sensitive to the completeness of the observed galaxy sample for given selection. Therefore, it is important to account for variations in the number of galaxies detected as a function of position on the sky and as a function of various instrument level patterns. The number of galaxies detected and the spectroscopic success rate could both be correlated with stellar density, extinction, sky brightness, air mass, position in the fibre plate etc. To remove these correlations, Ross et al. (2012) suggested the use of systematic weights. We use a different combination of systematic weights which is described in more detail in Bautista et al. (2018) for LRGs and Gil-Marín et al. (2018) for QSOs. Figure 3 investigates if such systematics affect our measurements for ELGs. We find that the measurement of w_p at small scales between 1–30 h^{-1}Mpc is insensitive to the details of such systematic weights and hence the results described in this paper are not prone to such systematics. We also note that fibre collisions lead to the galaxy sample becoming highly incomplete below the fibre scale marked by the vertical dashed line in Figure 3. There are several methods for correcting the clustering measurements at these scales (Anderson et al. 2012; Guo et al. 2012; Bianchi & Percival 2017). For the purpose of this paper we will not use these scales. We will perform this study in greater detail probing the very small scales by applying the method developed by Bianchi & Percival (2017) in a future work.

We measure galaxy environments following the method described in Alam et al. (2019), which we briefly summarise here. For galaxy survey one has to work with two catalogues. First a catalogue of galaxies containing the 3-dimensional location of each galaxy observed. Second, a catalogue of random positions representing the volume observed by the survey with the density of random points at any location representing survey completeness. In order to measure the galaxy

density we first count the number of random points in the Voronoi tessellation of the galaxy field. We then estimate the local density as the inverse of the random counts for each galaxy. This is then smoothed at the chosen scale to determine the smoothed density. The density is then converted to overdensity by first dividing by the mean density and then subtracting 1. In order to estimate the tidal environment of galaxies, we solve the Poisson equation as described in Section 3.3 of Alam et al. (2019) to obtain the tidal tensor, whose eigenvalues are then measured. We then define the tidal anisotropy (α_5) following Alam et al. (2019) as follows:

$$\alpha_5 = (1+\delta_5)^{-0.55}\sqrt{(\lambda_3-\lambda_2)^2+(\lambda_3-\lambda_1)^2+(\lambda_2-\lambda_1)^2}, \quad (17)$$

where $\lambda_{1,2,3}$ are the eigenvalues of the tidal tensor field and we adopt the convention that $\lambda_1 < \lambda_2 < \lambda_3$. The quantity δ_5 is the galaxy overdensity within a sphere of radius $5\,h^{-1}$Mpc centred on each galaxy. This form of tidal anisotropy was first proposed in Paranjape et al. (2018), and it determines the level of spherical anisotropy of the tidal field. The large value of α_5 corresponds to tidally anisotropic regions, and small values correspond to tidal isotropy. We always employ the same method to measure environment in data and mock catalogues, so that our comparisons are independent of any systematic uncertainty, for example the effects of smoothing scale or peculiar velocity.

By looking at the combination of δ_8 and α_5 we can assess the properties of galaxies in different parts of the cosmic web. For example, clusters live in regions with high δ_8 and low α_5, whereas voids will occupy regions with low δ_8 and low α_5. The regions with high α_5 will be filaments and we can probe the multi-scale nature of the cosmic web by looking at high-α_5 regions as the function of density. This will correspond to filaments that have different densities. Alam et al. (2019) suggested to use the scale of $5\,h^{-1}$Mpc for tidal anisotropy and $8\,h^{-1}$Mpc for over-density and shown that results are not very sensitive to these choices.

5 OBTAINING THE BEST FIT PARAMETERS

In this section, we describe the details of how we fit the model parameters and generate the predictions for the auto- and cross-correlations.

We are using the publicly available MultiDark Planck (MDPL2) simulation Prada et al. (2012) through the CosmoSim database [1]. MDPL is a dark matter only N-body simulation run using the Adaptive-Refinement-Tree (ART) code (Kravtsov et al. 1997). The simulation assumes a flat ΛCDM cosmology with $\Omega_m = 0.307$, $\Omega_b = 0.048$, $h = 0.67$, $n_s = 0.96$ and $\sigma_8 = 0.82$. The calculation adopts a periodic box of side $1000\,h^{-1}$Mpc and 3840^3 particles. The ART code used for MDPL is designed to preserve the physical resolution to $7\,h^{-1}$kpc for $z = 0-8$. A halo catalogue using the ROCKSTAR[2] halo finder (Behroozi et al. 2013) was constructed using the snapshot at an effective redshift of $z = 0.86$ for MDPL2. ROCKSTAR starts with a friends-of-friends group catalogue and analyses particles in full phase space (i.e. position and velocity) in order to define halo properties and robustly identify the substructures. We only use the main haloes in the halo catalogue, removing all the subhaloes and modelling satellite galaxies as described in Section 3.2.

We then use the models described in Section 3 to predict the number of central and satellite galaxies depending on the mass for all haloes in the catalogue, which are then populated to create a set of simulated catalogues, from which the projected correlation functions w_p are measured. The χ^2 fit is then performed using the measured w_p and jackknife covariance matrix. We then run a minimizer algorithm to find the parameters which give the minimum value of χ^2 and hence the best-fit HOD model. This process is repeated on only the auto-correlations of the individual tracers and we do not use the cross-correlations in the optimisation process. This is to test if the cross-correlation of galaxies is any different from the prediction based on the halo model estimated from the auto-correlations.

Parameters	LRG	QSO	ELG (erf)	ELG (HMQ)
$\log_{10}(M_c)$	13.0	12.21	11.88	11.75
σ_M	0.60	0.60	0.56	0.58
γ	-	-	-	4.12
Q	-	-	-	100
$\log_{10}(M_1)$	14.24	14.09	13.94	13.53
κ	0.98	1.0	1.02	1
α	0.40	0.39	0.40	1.0
$p_{\max}$	**0.33**	**0.033**	**0.33**	**0.33**

Table 1. The best fit `MTHOD` parameters for different tracers. The last column shows the ELG with HMQ model in which ELG galaxies are quenched at high mass haloes.

6 RESULTS

We fit the Multi-Tracer HOD (`MTHOD`) model initially only to the auto-correlation of LRG, ELG and QSO for our fiducial model, and we then compare the prediction of cross-correlations from our model to the observed results. We then discuss the signature of galactic conformity followed by the signature of the effect of the cosmic web on quenching efficiency. The projected auto-correlations of LRGs, QSOs and ELGs are fit between the scale of $1\,h^{-1}$Mpc and $30\,h^{-1}$Mpc. The best-fit model parameters for each tracer are shown in Table 1.

We first show the results of measurements and best-fit models in Figures 4 and 5. We show the halo occupation statistics of all three tracers for centrals and satellites in Figure 4. The plot on the left shows the occupation when ELGs are populated using the HMQ model and the one on the right shows the behaviour when ELGs are treated using the erf model. The shaded region represents the occupation probability of central galaxies, with grey area standing for LRGs, cyan for QSOs, blue for ELGs with erf model and red for ELGs with HMQ model. The dashed line shows the mean satellite occupation as a function of halo mass. This shows that the LRGs inhabit massive haloes compared with QSOs, whereas ELGs live in less massive haloes than QSOs. We also note that when ELG centrals are quenched in the

[1] https://www.cosmosim.org/cms/simulations/mdpl2/
[2] https://bitbucket.org/gfcstanford/rockstar

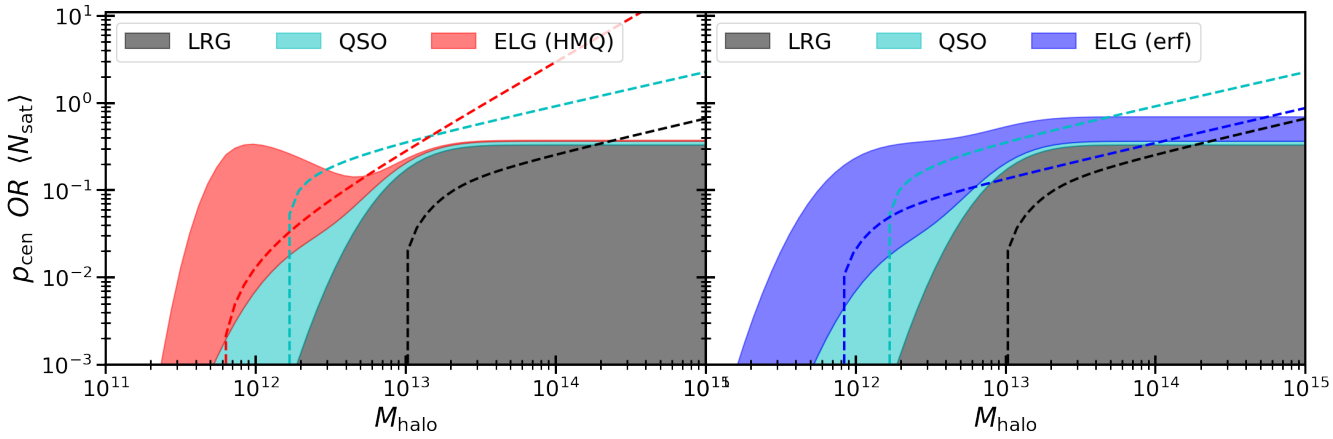

Figure 4. The best-fit occupation probability of galaxies as a function of halo mass in the MTHOD framework. The left panel is when ELG centrals are quenched in massive haloes (HMQ model) and the right panel is for no quenching in massive haloes for ELG (the erf model). The shaded region is the occupation probability of centrals and the dashed line represents the mean number of satellite galaxies. The black, cyan and blue colours are for LRG, QSO and ELG respectively. This shows that LRGs inhabit massive haloes compared to QSOs, whereas ELGs live in less massive haloes compared to QSOs.

massive haloes (using the HMQ model) then the mean occupation of satellites for ELGs in massive haloes increases (by comparing red dashed line in the left panel with the blue dashed line in the right panel of Figure 4). This suggests that quenching could trigger outflows of cold gas from halo centres, leading to increased star formation in the galaxies that are on the outskirts of massive haloes. Given the occupation probability we also note that it is very unlikely to have an ELG central and LRG satellite in the HMQ model because the distributions in halo mass are almost disjoint. Another interesting point to note is that in the left panel the total probability of a halo hosting a central galaxies has a peak at around $6 \times 10^{11}\, h^{-1} M_{\odot}$ and then a plateau for haloes with mass above $10^{13}\, h^{-1} M_{\odot}$. This implies that the total efficiency of galaxy formation for star forming eBOSS ELGs and eBOSS LRGs is suppressed around $3{\times}10^{12}\, h^{-1} M_{\odot}$. This probably arises from a combination of eBOSS selection and green valley galaxies dominating this intermediate halo mass.

The projected auto- and cross-correlations are shown in Figure 5. The top panels from left to right are for LRG, QSO and ELG auto-correlations. The bottom panels are for LRG×QSO, ELG×QSO and ELG×LRG cross-correlations from left to right. The x-axis is the projected separation and the y-axis is the projected correlation function multiplied by projected separation for clarity. The vertical dashed line in each panel indicates the fibre collision scale below which the clustering measurements are biased due to incomplete spectroscopic sample, and hence not used in this study. The black points are the observed eBOSS data with error bars estimated from the jackknife sub-sampling method. The black solid line shows the simple model where central galaxies of all three tracers are modelled by the erf function. The red solid line shows the model in which ELGs are quenched in high mass haloes. The orange dashed line in the cross-correlation plots shows the geometric mean of the auto-correlations. The numbers in square brackets within the legend wherever shown are [χ^2/dof] of the model. Both models provide an excellent fit to the auto-correlation. We can notice from the auto-correlation plot that the clustering amplitude of LRGs is highest, then QSOs followed by ELGs. This means that the bias of LRGs QSOs and ELGs will be ordered in declining order and hence that the mean halo mass will have a trend in the same direction. This is consistent with the picture from Figure 4, showing mean halo mass of ELGs (LRGs) is lower (higher) than mean halo mass of QSOs. We also note that the error on the ELG auto-correlation is smaller than for LRGs, with QSOs showing the largest error; this is because the number density of these tracers follows that order. The cross-correlation predicted by the best-fit model is consistent with observations. This means that no imprint of complicated formation mechanism of QSOs is detected in the eBOSS sample, given that the halo model predicts the cross-correlation of QSOs with both LRGs and ELGs at all measured scales. The cross-correlation predicted for ELG×LRG by our best-fit HMQ model shows a χ^2/dof = 31/16 and hence is not a good fit. This indicates that if the quenching in ELGs is driven by halo mass (as assumed in the HMQ model), then the occupation of LRGs and ELGs cannot be independent as assumed by the fiducial model. This is probably a signature of galactic conformity. The green line shows the model with 1-halo galactic conformity which improves the goodness of fit and is discussed in Section 6.2. Such an effect can possibly also arise by the distribution of satellite galaxies being different from NFW. We study a model in which LRG satellites has a factor of 2 higher concentration and ELG satellites a factor of 2 lower concentration shown by cyan solid line in Figure 5. We found that such a change in the model has no effect in the predicted signal and hence cannot explain the cross-correlation between LRGs and ELGs.

The number density of LRGs drops sharply above redshift of 0.9 as shown in Figure 1. Therefore, to understand if this has any effect on our measurement we repeated our measurements of LRG auto-correlation and its cross-correlation with ELGs and QSOs by selecting all galaxies within red-

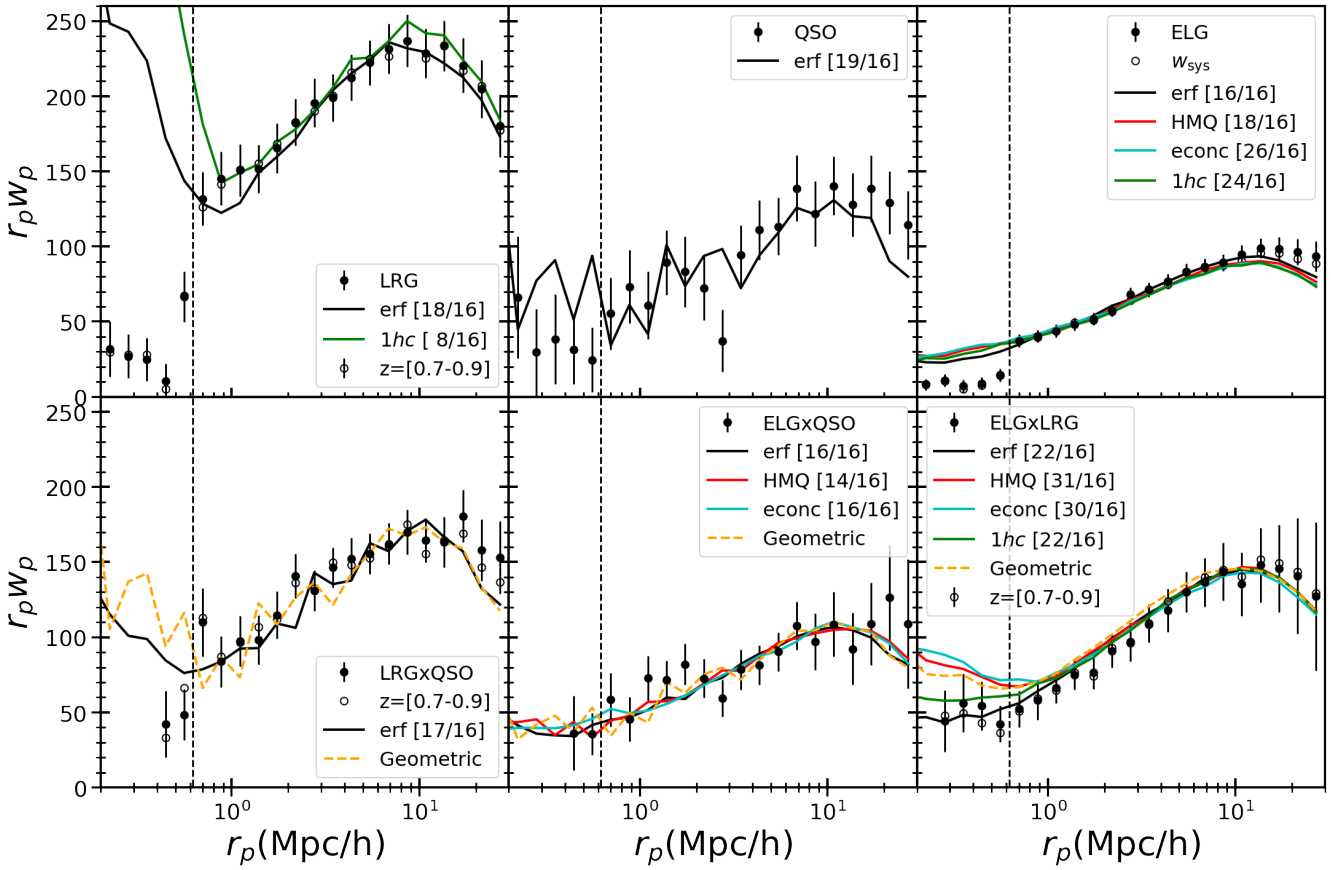

Figure 5. Projected correlation function $w_p(r_p)$ of auto- and cross-correlations for three tracers. The black points in each panel show the measurement from the eBOSS sample with jackknife errors. The black solid line shows the simple model where central galaxies in all three tracers are modelled by an error function. The red solid line shows the model in which ELGs are quenched in high mass haloes. The orange dashed line in the cross-correlation shows the geometric mean of auto-correlations. The green solid line shows a model with 1-halo conformity between ELG and LRG. The cyan solid line shows the model with stellite concentration for LRG (ELG) a factor of 2 higher (lower). The numbers in square brackets within the legend wherever shown are [χ^2/dof]. The black open circle in top-left, bottom-left and bottom-right are measurements from data with redshift cuts between 0.7 and 0.9. The black open circle in the top-right panel shows the ELG auto-correlation with systematic weights.

shift range of 0.7 and 0.9. The black open circles in the top left, bottom left and bottom right panels show the LRG auto-, LRG×QSO and ELG×LRG cross-correlations for this sub-sample respectively. This shows that restricted redshift selection and hence the sharp drop in LRG number-density at higher redshift does not affect our measurements. The systematic weights in ELG sample affect large-scale clustering significantly. Therefore, we also show the ELG auto-correlation with systematic weights by black open circles in the top right panel. This confirms that for the purpose our study in this paper the impact of systematic correlation of ELG number density with sky conditions is negligible.

6.1 Galaxy properties from MTHOD

Based on the MTHOD model we find that the luminous red galaxies in the eBOSS sample live in especially massive haloes, with 1% of the galaxies living in haloes with mass below $2.2\times10^{12}\,h^{-1}M_\odot$. Haloes of mass $2.8\times10^{15}\,h^{-1}M_\odot$ host on average one LRG satellite galaxy. The mean halo mass of the LRG sample is $1.9\times10^{13}\,h^{-1}M_\odot$. The LRG sample has a satellite fraction of 17%. Zhai et al. (2017) also studied an earlier version of the eBOSS LRG sample and found the mean halo mass of the sample to be $2.5\times10^{13}\,h^{-1}M_\odot$ with a satellite fraction of 13 ± 3%. The slightly higher mean halo mass and lower satellite fraction in Zhai et al. (2017) compared to our study can plausibly be understood as being due to the difference between our redshift cut of 0.7 compared to 0.6 used in the earlier study. Zhai et al. (2017) also showed that despite the possible incompleteness in the LRG sample, the HOD approach is sufficient to analyse this sample.

The QSOs in the eBOSS sample have lower bias than the LRGs and hence extend to lower halo masses than LRGs. The mean halo mass of the QSO sample is $5\times10^{12}\,h^{-1}M_\odot$, and 99% of QSOs in our sample are found in haloes with mass above $4.2\times10^{11}\,h^{-1}M_\odot$. The characteristic halo mass of satellite QSOs is $1.3\times10^{14}\,h^{-1}M_\odot$, for which the mean satellite number is 1. The QSO satellite fraction is 34%. Typically the form of the QSO HOD model is uncertain, but we expect our results not to be very sensitive to the parametric form of the HOD. The mean halo mass of the eBOSS QSO sample reported in Rodríguez-Torres et al. (2017) is $5\times10^{12}\,h^{-1}M_\odot$,

which is in agreement with our measurement despite a very different model. But our best-fit satellite fraction is much higher than generally reported in other QSO studies. We discuss the implication of such high QSO fractions and obtain more robust constraints in our companion paper (Alam et. al. in prep.).

The ELGs in the eBOSS sample are star-forming galaxies. We expect the galaxy quenching mechanism to be more effective in higher-mass haloes, so it is less likely for an ELG galaxy to be a central galaxy. We have used two different models for ELGs: the first one ('erf') does not have any effective quenching, but the second one ('HMQ') assumes galaxies to be quenched at high halo masses. Both models provide good fits to the auto-correlation of the ELG sample. The minimum halo mass required to cover 99% of ELG galaxies is $2.1\times10^{11}\,h^{-1}M_\odot$ for the erf model and $3.2\times10^{11}\,h^{-1}M_\odot$ for the HMQ model. The mean halo mass of the ELG sample is $2.9\times10^{12}\,h^{-1}M_\odot$ for the erf model and $1.1\times10^{12}\,h^{-1}M_\odot$ for the HMQ model. The characteristic satellite halo masses are $1.4\times10^{15}\,h^{-1}M_\odot$ for erf and $3.6\times10^{13}\,h^{-1}M_\odot$ for HMQ. The satellite fraction of the ELG sample is 12% and 17% for the erf and HMQ models, respectively. One interesting point this raises concerns the minimum halo mass that one would require in order to host an ELG. In the HMQ model the mean halo mass of an ELG is 3 times lower than in the erf model. This means for future surveys like DESI the simulation requirement could have significant impact on the resolution requirement, given that the minimum host halo mass of 99% of the ELG sample could be higher by a factor of 2 for the more physical HMQ model. Guo et al. (2019) report that the mean halo mass of ELGs is $10^{12}\,h^{-1}M_\odot$ with a satellite fraction between 13% to 17%, consistent with the results obtained in this paper.

6.2 Galactic conformity

Galactic conformity is usually identified in observations by studying the colours or star formation rates of galaxies, and quantified in terms of red (quiescent) fractions and/or quenching efficiencies. In testing the concept of galactic conformity, it is crucial to compare samples that have been matched in one or more parameters in order to avoid trivially arising correlations. Following the probabilistic description of the meaning of galactic conformity, put forward by Knobel et al. (2015), this phenomenon can be seen as arising due to one or more *hidden variables* not accounted for in the analysis. Among obvious candidates for these potential hidden parameters that have been addressed in previous studies are the luminosity, stellar mass, halo mass of galaxies or their local density. None of them has been identified as a principal driver of the observed phenomenon.

Numerical simulations allow us to extend the range of explored parameters to properties that are not easily accessible in the observed data sets, such as age or formation history of galaxies and their haloes. Using the Illustris (Vogelsberger et al. 2014) simulation, Bray et al. (2016) confirmed a significant signal of galactic and halo conformity out to distances of about 10 Mpc that coupled with a galaxy colour-halo age relation, resulting in the reddest galaxies preferentially residing in the oldest haloes. The interpretation of galactic conformity in this picture is that dark matter clustering is the primary factor, but a sufficiently tight galaxy colour-halo age relation is necessary in order to measure the conformity signal. Similarly, Rafieferantsoa & Davé (2018) found that the cosmological hydrodynamical simulation Mufasa (Davé et al. 2016) produces conformity in various galaxy properties at fixed halo mass, with the *1-halo* term dominating the signal.

Commonly discussed interpretations of galactic conformity seen in the data, on large scales in particular, invoke assembly bias leading to the dependence of galaxy properties on the properties of a halo beyond its mass. Among these, halo age and concentration correlated with galaxy colour or star formation history were found to reproduce the galactic conformity in analytical models based on the HOD framework (e.g. Hearin et al. 2015; Paranjape et al. 2015; Pahwa & Paranjape 2017). On the other hand, using the HOD halo quenching framework of Zu & Mandelbaum (2015, 2016), Zu & Mandelbaum (2018) showed that the galaxy conformity seen in the SDSS data can be naturally explained by the combination of halo quenching and the variation of the halo mass function with environment, without the need for any galaxy assembly bias. This is consistent with the findings of Tinker et al. (2018), who compared the conformity in the SDSS with the predictions from the halo age-matching model and concluded that it can be produced by mechanisms other than halo assembly bias, e.g. difference in halo mass at fixed stellar mass for blue (star-forming) and red (passive) galaxies. Such a bimodality is suggested by the weak lensing measurements of bright galaxies in the SDSS, where at fixed stellar mass, red centrals are found to preferentially reside in more massive haloes than blue ones (Zu & Mandelbaum 2016). Applying such a colour dependent halo-to-stellar-mass ratio (e.g. Zu & Mandelbaum 2015) to estimate the halo mass of galaxies in the GAMA survey, Treyer et al. (2018) recently showed that conformity at fixed halo mass indeed vanishes.

Galactic conformity will cause the cross-correlation of LRGs and ELGs to differ from the behaviour expected in a universe without such conformity. We detect a signature of a failure of our fiducial model (which lacks conformity effects) to describe the cross-correlation of ELG and LRG samples. Therefore we introduce an explicit *1-halo* and *2-halo* galactic conformity in our model to constrain this effect. One of the major systematics for conformity studies in the past was uncertainty in the identification of central and satellite galaxies. We avoid such issues by introducing conformity in our model only where we precisely know which galaxies are centrals and satellites, and comparing only the overall auto- and cross-correlations.

6.2.1 1-halo galactic conformity

We therefore introduce an additional parameter in our model denoted by $f_{\rm conf}$, which represents the level of galactic conformity. In this model we say that in all haloes with an LRG as a central galaxy, a certain fraction of ELG satellites will be turned into LRGs. Mathematically this can be written as follows for haloes with an LRG as the central galaxy:

$$\left\langle N_{\rm sat}^{\rm LRG,conf}\right\rangle = \left\langle N_{\rm sat}^{\rm LRG}\right\rangle + f_{\rm conf}\left\langle N_{\rm sat}^{\rm ELG}\right\rangle, \tag{18}$$

$$\left\langle N_{\rm sat}^{\rm ELG,conf}\right\rangle = (1-f_{\rm conf})\left\langle N_{\rm sat}^{\rm ELG}\right\rangle. \tag{19}$$

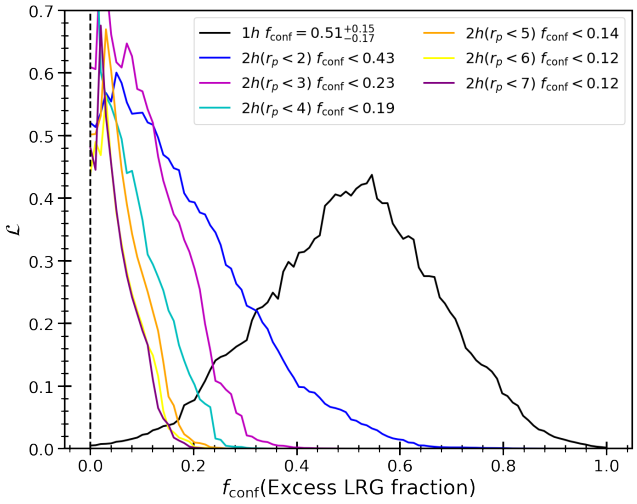

Figure 6. Likelihood of the galactic conformity parameter $f_{\rm conf}$. The black dashed line represents the zero conformity model. The black solid line shows the *1-halo* conformity constraints and other coloured solid lines are for *2-halo* conformity at different scales as shown in the legend. We also provide 68% constraint for *1-halo* conformity and 95% upper limit for *2-halo* conformity in the legend.

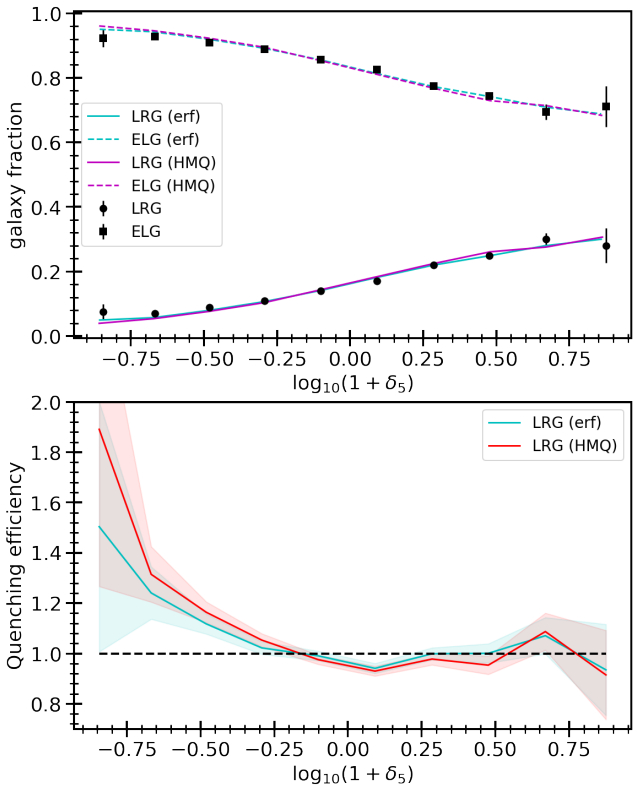

Figure 7. The environmental dependence of galaxy quenching. The top panel shows the fraction of ELGs and LRGs as a function of environmental overdensity for the observed data with black points, and model predictions with coloured lines. The bottom panel shows the excess quenching efficiency with observed overdensity compared to models.

We do not enforce a number density constraint here due to the large uncertainty in the number density; the impact of this change is small compared to the uncertainty. One can also argue using a more complicated model of conformity. But here we limit ourselves to this simple model due to lack of any strong motivation for something more complicated. We first look at all haloes with LRG centrals and count the total number of ELG satellites in such haloes. We then randomly convert a fraction $f_{\rm conf}$ of those ELG satellites into LRGs. This model is then fitted to the projected correlation function of LRG, ELG and ELG×LRG, thus determining the relative likelihood as a function of $f_{\rm conf}$. Figure 6 shows the likelihood of $f_{\rm conf}$ for the *1-halo* conformity signal with a black solid line. We measure $f_{\rm conf} = 0.51^{+0.15}_{-0.17}$, a 3σ detection of *1-halo* galactic conformity at a mean redshift of 0.86. One of the consequences of *1-halo* conformity is that it changes the satellite fraction of the sample. The best fit model with quenching shows satellite fraction of 20.7% and 16.6% for LRGs and ELGs respectively. Whereas the model without conformity showed satellite fraction of 17% for both LRGs and ELGs.

The *1-halo* conformity is typically compared at fixed halo mass (e.g. Treyer et al. 2018). In this work we do not control for the halo mass due to difficulties in obtaining such measurements. The conformity model introduced in this work allows for galactic conformity only in haloes with central galaxies that are LRGs, which have a mean halo mass of $1.9 \times 10^{13}\, h^{-1} M_\odot$. Therefore, the halo mass for *1-halo* conformity is being fixed indirectly using the mean mass of LRGs.

6.2.2 2-halo galactic conformity

We now use the same parameter $f_{\rm conf}$ to model *2-halo* galactic conformity. In this case we again look at all LRG centrals and count the number of ELGs (both centrals and satellites) within a given distance of the central LRG galaxies. The model then demands that a fraction $f_{\rm conf}$ of those ELGs should be turned randomly into LRGs. This modified galaxy catalogue is then used to measure the clustering, which is fitted to constrain $f_{\rm conf}$. Figure 6 shows the likelihood of $f_{\rm conf}$ for *2-halo* conformity as a function of scale. We do not detect any *2-halo* galactic conformity signal, and only obtain an upper limit on the possible size of the effect. The legend in the plot quotes 95% upper limit on the *2-halo* galactic conformity parameter.

6.3 Galaxy quenching and environment

The environmental dependence of galaxy properties is one of the key aspects of the galaxy formation process. In general the properties of galaxies strongly correlate with their host halo mass and overdensity, reflecting the variation of the gravitational potential with their location. As the major force during galaxy formation is gravity, the local dark matter density or the host dark matter halo of galaxies are expected to drive their properties, in particular governing the extent of quenching. However, most hydrodynamical simulations predict that at some point baryonic physics should play a role, so that such processes need to be accounted for in addition to the dark matter halo mass in order to under-

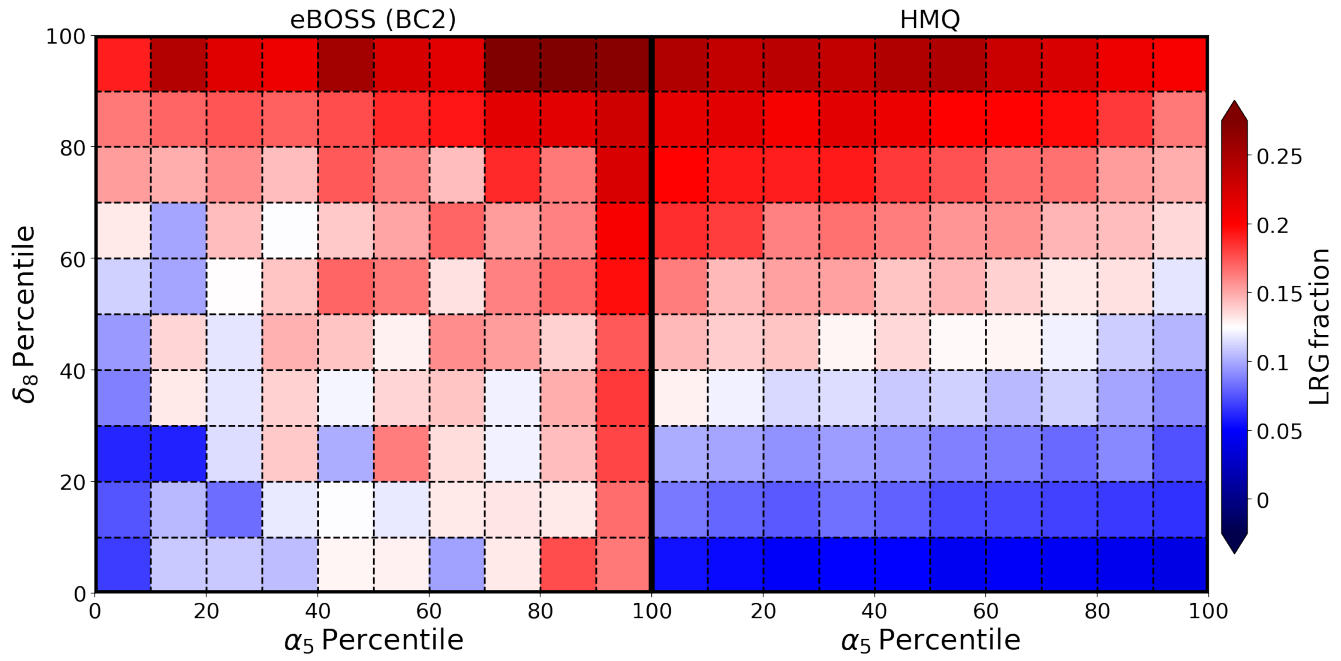

Figure 8. Comparison of the LRG fraction between eBOSS (left) and HMQ (right) galaxies in the $\delta_8 - \alpha_5$ plane. Each cell is colour-coded by the fraction of LRGs compared to all galaxies in 2D bins of ten percentiles in δ_8 and α_5 jointly. The subtle dependence of the LRG fraction on δ_8 mostly reflects halo mass driven quenching as it is reproduced in the HMQ results, but the dependence on α_5 is probably the evidence for a tidal dependence of galaxy quenching. The typical errors in the LRG fractions are 0.02 for data and 0.005 for HMQ model.

stand galaxy quenching. But given that such processes are second order, the net effect is often small and hard to disentangle from the dependence on the dark matter only (Alam et al. 2019).

Therefore we make a detailed comparison between the observed eBOSS sample and the `MTHOD` model, the simple form of which assumes quenching to be driven by halo mass alone. First we measure the LRG fraction as a function of density contrast (δ_8) in data and in the two mocks using the method described in Section 4. We show LRG and ELG fractions with overdensity in the top panel of Figure 7 with black points for the eBOSS sample and with coloured solid lines for different models. If we think of the fraction of LRGs in a given environment as an indicator of quenching efficiency, then from this plot we first show that the galaxy quenching efficiency strongly depends on the dark matter overdensity – a trend that is also reproduced by the `MTHOD` catalogue as shown with the coloured lines. The fact that the `MTHOD` catalogue shows a reasonable agreement with the data means that the dominant terms causing this dependence must arise from the dark matter halo mass. We note that in high-density environments the data and models agree very closely, meaning that galaxy quenching is mainly driven by halo mass in these regions of high density. However, in low density environments the data exhibit more efficient quenching than the model predicts. This is highlighted further in the bottom panel of Figure 7, showing the ratio of the observed LRG fraction with respect to the model. The bottom panel shows that the galaxy quenching efficiency is higher in the data by up to a factor of 1.5 for the more physical HMQ model, and by a factor of 1.2 in the erf model. In addition, the quenching efficiency around the mean density is lower in the data than in the mocks. This is possibly caused by the fact that the material in under-dense regions will deplete faster than in higher density regions due to outflows; thus the quenching efficiency is enhanced. This also results in slightly less efficient quenching in the mean density regions due to the transfer of extra gas from low density regions to the mean density regions.

We further ask more specifically whether quenching of galaxies is influenced by *geometrical* location within the cosmic web. The accretion of gas onto haloes can depend on the tidal environment of the haloes. This can cause a further dependence of quenching efficiency on tidal environment, in addition to the effect of halo mass (Kereš et al. 2005). To investigate whether any cosmic web quenching exists, we look at the fraction of LRGs in different cosmic web environments, defined by δ_8 and α_5. We first evaluate δ_8 and α_5 values for both data and mocks, following the method described in section 4. We then split the galaxies into 10 percentile bins of δ_8 and α_5 jointly. For each such cell, the fraction of LRGs is estimated by taking the ratio of the number of LRGs to the number of all galaxies in the given cell. This 10×10 matrix of LRG fractions is shown in Figure 8, where the x-axis is for the α_5 percentile and the y-axis is for the δ_8 percentile. The left panel shows the 2D LRG fraction measured from eBOSS data and the right panel shows the corresponding result derived from the HMQ mocks. Note that the tidal anisotropy (α_5) is by construction independent of δ_8 (see Figure A2 for details). It is clear that the observed LRG fraction depends on both δ_8 and α_5 simulta-

neously, showing several interesting features in the δ_8 vs. α_5 plane:

- The high-density filaments (high δ_8 and high α_5) and clusters (high δ_8 and low α_5) show strong quenching efficiency in both data and model. But the data show slightly lower quenching efficiencies in clusters compared to high-density filaments, whereas the model shows slightly higher quenching efficiencies in clusters compared to the data. This implies that the quenching efficiency in high-density regions is largely driven by halo mass, with additional small effects from the cosmic web in the filaments.
- The observed quenching efficiency in void regions (low δ_8 and low α_5) is small and is similar to the quenching efficiency in the mock. Therefore, the quenching efficiency in voids can be explained by halo mass driven quenching.
- The observed quenching efficiency in filaments (high α_5) is high and shows a weak positive correlation with density (δ_8). This is in contrast with the mock assuming halo mass driven quenching, which predicts the quenching efficiency in filaments to correlate strongly with density (δ_8). This suggests that the cosmic web has a significant impact on the quenching efficiency in low-density filaments.
- Galaxies in mean density isotropic regions (intermediate δ_8 and low α_5) show lower quenching efficiency in the data compared to the model predictions.

The halo mass driven quenching produces a quenching efficiency map with a complicated dependence on cosmic web properties, as shown in the right panel of Figure 8. This matches the observed quenching efficiency map (shown in the left panel of Figure 8) over most of the parameter plane. But it under-predicts the quenching efficiency in the low-density filaments. This implies that either the galaxy quenching efficiency for-low density filaments is driven by mechanisms beyond halo mass quenching, or possibly that the star forming galaxies in low-density filaments occupy different part of colour-magnitude space compared to other star-forming galaxies. Either way this is an interesting signature, showing the impact of the cosmic web on galaxy formation and evolution.

7 SUMMARY AND DISCUSSION

We have extended the halo occupation distribution model into a form suitable for application to multiple tracers in ongoing and future surveys: the Multi-Tracer HOD (`MTHOD`). The model by default includes the environmental dependence of the halo mass function by using numerical halo catalogues from N-body simulations to construct mock galaxy data sets. We propose a new parametric form for the occupation probability of star-forming galaxies, which allows the incorporation of quenching physics: the HMQ model (see equation 9). We apply this `MTHOD` framework to the eBOSS data within the redshift range 0.7–1.1. We first obtain halo model constraints for three kinds of tracers in the eBOSS sample: LRGs, ELGs and QSOs. We compare our results with earlier efforts to model these samples, finding generally good agreement. The mean halo masses of LRGs and QSOs are $1.9 \times 10^{13}\, h^{-1} M_\odot$ and $5 \times 10^{12}\, h^{-1} M_\odot$ respectively, in agreement with previous studies (Zhai et al. 2017; Rodríguez-Torres et al. 2017). Within the HMQ model, the mean halo mass of ELGs is found to be $1.1 \times 10^{12}\, h^{-1} M_\odot$. We also note that in the absence of any quenching at the centres of massive haloes the mean halo mass is a factor of 3 larger for ELGs.

We then focus on the cross-correlations between different tracers, comparing our model with the data. The overall cross-correlations are in very good agreement at large scales. The cross-correlation of QSOs with ELGs (star-forming) and LRGs (quenched) is completely consistent with the prediction from the `MTHOD` models. We see no signature of the eBOSS QSOs being especially located around star-forming galaxies within the statistical error in the data. This supports the arguments that QSOs are formed in typical galaxies.

However, we found that the cross-correlation between LRGs and ELGs at small scales is not in such good agreement with our fiducial model. The deviation between the observed cross-correlation and prediction is limited to scales below $5\, h^{-1}$Mpc, which is similar to the signature of galactic conformity. We hypothesise that this deviation reflects the presence of galactic conformity in the observed sample. We introduce galactic conformity within the `MTHOD` framework as described in Section 6.2. We compared the resulting predicted cross-correlation with the data, obtaining consistent results (see the green line in Figure 5). This indicates the detection of *1-halo* galactic conformity at the 3σ level, although no signature of a conformity effect in the *2-halo* regime was detected (see Figure 6). We also looked at the possibility that the deviation in the cross-correlation might arise simply because the concentration of LRG and ELG satellites are respectively smaller and larger than the concentration of the host dark matter haloes. We created a mock catalogue with double the satellite concentration for ELGs and half the satellite concentration for LRGs. The resulting cross-correlation is not different at the relevant scale and could not explain the galactic conformity signal. Thus the *1-halo* galactic conformity signal we observe cannot be the result of differences in the satellite galaxy distributions within dark matter haloes.

We then study the environmental dependence of quenching by comparing the fraction of LRGs as a function of the cosmic web environment between the observed data and the `MTHOD` mock galaxy catalogue. The cosmic web is characterised by galaxy over-density (δ_8) and tidal anisotropy (α_5) at the position of each galaxy. The estimate of the tidal anisotropy (α_5) for galaxies around the survey boundary may become unreliable. We show the impact of boundary effects in Appendix A and remove galaxies around survey boundaries in order to avoid any bias in our results. We show that in the high density regime the halo mass driven quenching in the `MTHOD` model is consistent with observations. But in lower density regions we find that the observed quenching efficiency shows a deviation from halo mass driven quenching. We found that the quenching efficiency in the `MTHOD` model is smaller by a factor of 1.5 compared to the observed data in under-dense regions (see Figure 7).

To understand if the difference in quenching efficiency arises from any specific tidal environment, we study the LRG fraction in the two-dimensional space of density and tidal anisotropy as shown in Figure 8. We found that the observed galaxy quenching efficiency depends on both overdensity as

well as tidal anisotropy. The quenching efficiency in clusters, voids and high density filaments is consistent between observed data and our mock catalogue. This suggests that in such parts of cosmic web, galaxy quenching is well explained by the halo mass driven quenching model. But the quenching efficiency in the low-density filaments is predicted to be much smaller than the observed effect. This suggest that either the galaxy quenching efficiency is driven by tidal fields beyond halo mass in the low-density filaments, or that the OII-bright star-forming galaxies (ELGs) observed by eBOSS avoid low-density filaments due to the impact of cosmic web on galaxy formation. In any case this is a clear signature of tidal fields playing a role in the galaxy formation process and dominating in the low-density filaments. The role of the filaments, beyond that of density, was recently highlighted by works showing that red or high-mass galaxies tend to be closer to the filaments than blue or low-mass and late-forming galaxies (Chen et al. 2017; Malavasi et al. 2017; Kraljic et al. 2018; Laigle et al. 2018). There is also some evidence that low mass late-type galaxies tend to have lower neutral gas content near the filament spine (Crone Odekon et al. 2018), suggesting that galaxies are cut off from their supply of cold gas in this environment. Massive galaxies on the other hand seem to show evidence of increased cold gas content in the vicinity of filaments (Kleiner et al. 2017), providing support for cold mode accretion where galaxies with a large gravitational potential can draw gas from large-scale structure. The exact mechanism by which galaxies are quenched in the vicinity of the cosmic web filaments is still highly debated. It could be driven by the cosmic web detachment (Calvo et al. 2019), where the cut-off of gas supplies near and inside filaments is caused by the turbulent regions inside filaments. Another interpretation is based on the cold gas accretion controlled by the filamentary structure (Pichon et al. 2011; Codis et al. 2015; Laigle et al. 2015; Welker et al. 2017), where the most efficient helicoidal infall of cold gas is expected in the outskirts of filaments. Our result showing a beyond halo mass effect driving quenching in low-density filaments is first where filaments are split by density. A detailed comparison with a suite of full hydrodynamic simulations should provide insight on the physical mechanism of quenching beyond halo mass.

One of the main limitations of this work with regards to constraining galaxy physics is the lack of small scale information due to fibre collisions in the observed data. The cross-correlation at small scales is expected to be especially sensitive to the impact of the cosmic web as well as to the inter-dependence of different tracers. Measurement at smaller scales could potentially boost the results in this paper to much higher significance and we hope to address this regime in future studies.

In summary, the extended halo model is quite powerful in understanding galaxy properties. It has allowed us to detect a clean signature of *1-halo* galactic conformity. It also shows that galaxy quenching can be explained by a model with halo mass driven quenching in most parts of the cosmic web (clusters, voids and high density filaments). But the quenched galaxy fraction in the low-density filaments is not as predicted by the halo mass quenching model. Our fiducial `MTHOD` model with its variants incorporating galaxy properties beyond those due to halo mass will thus be fundamental for calibrating models of redshift space distortions used to obtain cosmological constraints, and to assess the systematic biases that may arise from the presence of such additional effects.

ACKNOWLEDGEMENTS

SA and JAP are supported by the European Research Council through the COSFORM Research Grant (#670193). We thank Horst Meyerdierks and Eric Tittley for their support with Stacpolly and Cuillin cluster where all of the computing for this project is performed. SA would like to thank Ravi K. Sheth for constructive discussions. We also thank anonymous referee for constructive comments on the initial draft. We thank the Multi Dark Patchy Team for making their simulations publicly available. This research has made use of NASA's Astrophysics Data System.

Funding for the Sloan Digital Sky Survey IV has been provided by the Alfred P. Sloan Foundation, the U.S. Department of Energy Office of Science, and the Participating Institutions. SDSS-IV acknowledges support and resources from the Center for High-Performance Computing at the University of Utah. The SDSS web site is www.sdss.org.

SDSS-IV is managed by the Astrophysical Research Consortium for the Participating Institutions of the SDSS Collaboration including the Brazilian Participation Group, the Carnegie Institution for Science, Carnegie Mellon University, the Chilean Participation Group, the French Participation Group, Harvard-Smithsonian Center for Astrophysics, Instituto de Astrofísica de Canarias, The Johns Hopkins University, Kavli Institute for the Physics and Mathematics of the Universe (IPMU) / University of Tokyo, the Korean Participation Group, Lawrence Berkeley National Laboratory, Leibniz Institut für Astrophysik Potsdam (AIP), Max-Planck-Institut für Astronomie (MPIA Heidelberg), Max-Planck-Institut für Astrophysik (MPA Garching), Max-Planck-Institut für Extraterrestrische Physik (MPE), National Astronomical Observatories of China, New Mexico State University, New York University, University of Notre Dame, Observatário Nacional / MCTI, The Ohio State University, Pennsylvania State University, Shanghai Astronomical Observatory, United Kingdom Participation Group, Universidad Nacional Autónoma de México, University of Arizona, University of Colorado Boulder, University of Oxford, University of Portsmouth, University of Utah, University of Virginia, University of Washington, University of Wisconsin, Vanderbilt University, and Yale University.

The CosmoSim database used in this paper is a service by the Leibniz-Institute for Astrophysics Potsdam (AIP). The MultiDark database was developed in cooperation with the Spanish MultiDark Consolider Project CSD2009-00064.

The authors gratefully acknowledge the Gauss Centre for Supercomputing e.V. (www.gauss-centre.eu) and the Partnership for Advanced Supercomputing in Europe (PRACE, www.prace-ri.eu) for funding the MultiDark simulation project by providing computing time on the GCS Supercomputer SuperMUC at Leibniz Supercomputing Centre (LRZ, www.lrz.de).

8 DATA AVAILABILITY

All of the observational data used in this paper is available through the SDSS website https://data.sdss.org/sas/dr16/eboss/. The codes used in this analysis along with instructions are available on https://www.roe.ac.uk/~salam/MTHOD/.

REFERENCES

Abazajian K. N., et al., 2009, ApJS, 182, 543
Alam S., Zu Y., Peacock J. A., Mand elbaum R., 2019, MNRAS, 483, 4501
Anderson L., et al., 2012, MNRAS, 427, 3435
Baldry I. K., Glazebrook K., Brinkmann J., Ivezić Ž., Lupton R. H., Nichol R. C., Szalay A. S., 2004, ApJ, 600, 681
Balogh M. L., Baldry I. K., Nichol R., Miller C., Bower R., Glazebrook K., 2004, ApJ, 615, L101
Bautista J. E., et al., 2018, ApJ, 863, 110
Behroozi P. S., Wechsler R. H., Wu H.-Y., 2013, ApJ, 762, 109
Benson A. J., Cole S., Frenk C. S., Baugh C. M., Lacey C. G., 2000, MNRAS, 311, 793
Berlind A. A., Weinberg D. H., 2002, ApJ, 575, 587
Berti A. M., Coil A. L., Behroozi P. S., Eisenstein D. J., Bray A. D., Cool R. J., Moustakas J., 2017, ApJ, 834, 87
Bianchi D., Percival W. J., 2017, MNRAS, 472, 1106
Blanton M. R., et al., 2017, AJ, 154, 28
Borzyszkowski M., Porciani C., Romano-Díaz E., Garaldi E., 2017, MNRAS, 469, 594
Bovy J., et al., 2012, ApJ, 749, 41
Bray A. D., et al., 2016, MNRAS, 455, 185
Calderon V. F., Berlind A. A., Sinha M., 2018, MNRAS, 480, 2031
Calvo M. A. A., Neyrinck M. C., Silk J., 2019, The Open Journal of Astrophysics, 2
Castorina E., Paranjape A., Hahn O., Sheth R. K., 2016, preprint, (arXiv:1611.03619)
Cattaneo A., Dekel A., Devriendt J., Guiderdoni B., Blaizot J., 2006, MNRAS, 370, 1651
Chen Y.-C., et al., 2017, MNRAS, 466, 1880
Codis S., Pichon C., Pogosyan D., 2015, MNRAS, 452, 3369
Comparat J., et al., 2013a, MNRAS, 428, 1498
Comparat J., et al., 2013b, MNRAS, 433, 1146
Comparat J., et al., 2015, A&A, 575, A40
Comparat J., et al., 2016, A&A, 592, A121
Cooray A., 2006, MNRAS, 365, 842
Cooray A., Sheth R., 2002, Phys. Rep., 372, 1
Correa C. A., Schaye J., Wyithe J. S. B., Duffy A. R., Theuns T., Crain R. A., Bower R. G., 2018, MNRAS, 473, 538
Crone Odekon M., Hallenbeck G., Haynes M. P., Koopmann R. A., Phi A., Wolfe P.-F., 2018, ApJ, 852, 142
DESI Collaboration et al., 2016, arXiv e-prints, p. arXiv:1611.00036
Davé R., Thompson R., Hopkins P. F., 2016, MNRAS, 462, 3265
Dawson K. S., et al., 2013, AJ, 145, 10
Dawson K. S., et al., 2016, AJ, 151, 44
Dekel A., Birnboim Y., 2006, MNRAS, 368, 2
Dey A., et al., 2019, AJ, 157, 168
Eisenstein D. J., et al., 2011, AJ, 142, 72
Favole G., et al., 2016, MNRAS, 461, 3421
Georgakakis A., Comparat J., Merloni A., Ciesla L., Aird J., Finoguenov A., 2019, MNRAS, 487, 275
Gil-Marín H., et al., 2018, MNRAS, 477, 1604
Gonzalez-Perez V., et al., 2018, MNRAS, 474, 4024
Gunn J. E., et al., 2006, AJ, 131, 2332
Guo H., Zehavi I., Zheng Z., 2012, ApJ, 756, 127
Guo H., et al., 2015, MNRAS, 453, 4368
Guo H., et al., 2019, ApJ, 871, 147
Hahn O., Porciani C., Dekel A., Carollo C. M., 2009, MNRAS, 398, 1742
Hartley W. G., Conselice C. J., Mortlock A., Foucaud S., Simpson C., 2015, MNRAS, 451, 1613
Hearin A. P., Watson D. F., van den Bosch F. C., 2015, MNRAS, 452, 1958
Kauffmann G., et al., 2003, MNRAS, 341, 54
Kauffmann G., Li C., Heckman T. M., 2010, MNRAS, 409, 491
Kauffmann G., Li C., Zhang W., Weinmann S., 2013, MNRAS, 430, 1447
Kawinwanichakij L., et al., 2016, ApJ, 817, 9
Kereš D., Katz N., Weinberg D. H., Davé R., 2005, MNRAS, 363, 2
Kleiner D., Pimbblet K. A., Jones D. H., Koribalski B. S., Serra P., 2017, MNRAS, 466, 4692
Knobel C., Lilly S. J., Woo J., Kovač K., 2015, ApJ, 800, 24
Kraljic K., et al., 2018, MNRAS, 474, 547
Kravtsov A. V., Klypin A. A., Khokhlov A. M., 1997, ApJS, 111, 73
Lacerna I., Contreras S., González R. E., Padilla N., Gonzalez-Perez V., 2018, MNRAS, 475, 1177
Laigle C., et al., 2015, MNRAS, 446, 2744
Laigle C., et al., 2018, MNRAS, 474, 5437
Landy S. D., Szalay A. S., 1993, ApJ, 412, 64
Lang D., Hogg D. W., Schlegel D. J., 2014, arXiv e-prints, p. arXiv:1410.7397
Liske J., et al., 2015, MNRAS, 452, 2087
Malavasi N., et al., 2017, MNRAS, 465, 3817
Musso M., Cadiou C., Pichon C., Codis S., Kraljic K., Dubois Y., 2018, MNRAS,
Myers A. D., et al., 2015, ApJS, 221, 27
Pahwa I., Paranjape A., 2017, MNRAS, 470, 1298
Paranjape A., Kovač K., Hartley W. G., Pahwa I., 2015, MNRAS, 454, 3030
Paranjape A., Hahn O., Sheth R. K., 2018, MNRAS, 476, 3631
Peacock J. A., Smith R. E., 2000, MNRAS, 318, 1144
Phillips J. I., Wheeler C., Boylan-Kolchin M., Bullock J. S., Cooper M. C., Tollerud E. J., 2014, MNRAS, 437, 1930
Pichon C., Pogosyan D., Kimm T., Slyz A., Devriendt J., Dubois Y., 2011, MNRAS, 418, 2493
Prada F., Klypin A. A., Cuesta A. J., Betancort-Rijo J. E., Primack J., 2012, MNRAS, 423, 3018
Prakash A., Licquia T. C., Newman J. A., Rao S. M., 2015, ApJ, 803, 105
Prakash A., et al., 2016, ApJS, 224, 34
Rafieferantsoa M., Davé R., 2018, MNRAS, 475, 955
Raichoor A., et al., 2017, MNRAS, 471, 3955
Raichoor et al., 2020, in prep.
Richardson J., Zheng Z., Chatterjee S., Nagai D., Shen Y., 2012, ApJ, 755, 30
Robotham A. S. G., et al., 2013, MNRAS, 431, 167
Rodríguez-Torres S. A., et al., 2017, MNRAS, 468, 728
Ross A. J., Brunner R. J., 2009, MNRAS, 399, 878
Ross A. J., et al., 2012, MNRAS, 424, 564
Ross A., et al., 2020, in prep.
Scranton R., 2002, MNRAS, 332, 697
Seljak U., 2000, MNRAS, 318, 203
Sin L. P. T., Lilly S. J., Henriques B. M. B., 2017, MNRAS, 471, 1192
Skibba R. A., Sheth R. K., 2009, MNRAS, 392, 1080
Smee S. A., et al., 2013, AJ, 146, 32
Strateva I., et al., 2001, AJ, 122, 1861
Tinker J. L., Hahn C., Mao Y.-Y., Wetzel A. R., Conroy C., 2018, MNRAS, 477, 935
Treyer M., et al., 2018, MNRAS, 477, 2684
Vogelsberger M., et al., 2014, MNRAS, 444, 1518
Wang W., White S. D. M., 2012, MNRAS, 424, 2574

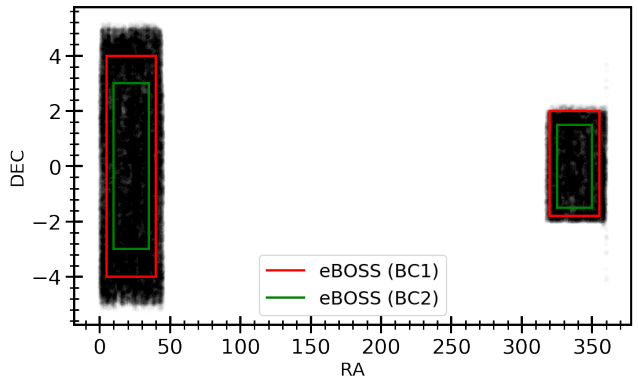

Figure A1. The sky coverage of the full sample is shown in the black and the green and red lines show the boundary cuts used to create the BC1 and BC2 sub-samples respectively.

Weinmann S. M., van den Bosch F. C., Yang X., Mo H. J., 2006, MNRAS, 366, 2
Welker C., Dubois Y., Devriendt J., Pichon C., Kaviraj S., Peirani S., 2017, MNRAS, 465, 1241
White M., Hernquist L., Springel V., 2001, ApJ, 550, L129
Wright E. L., et al., 2010, AJ, 140, 1868
Xu H., Zheng Z., Guo H., Zu Y., Zehavi I., Weinberg D. H., 2018, MNRAS, 481, 5470
Zhai Z., et al., 2017, ApJ, 848, 76
Zheng Z., et al., 2005, ApJ, 633, 791
Zu Y., Mandelbaum R., 2015, MNRAS, 454, 1161
Zu Y., Mandelbaum R., 2016, MNRAS, 457, 4360
Zu Y., Mandelbaum R., 2018, MNRAS, 476, 1637

APPENDIX A: GALAXY ENVIRONMENT AND SURVEY BOUNDARIES

For a real survey the estimates of density and tidal field can be contaminated around the survey boundary. Therefore to investigate such effects we created various datasets with different degrees of exclusion of galaxies at the boundary. First we create two sub-samples of our galaxies by removing galaxies around boundaries called BC1 and BC2. Figure A1 shows the sky distribution of all galaxies in our sample in black. The two boundary cuts are shown with red and green lines respectively. For each of these sub-samples we first look at the distribution of overdensity and tidal anisotropy. Figure A2 shows the two dimensional and marginalised one dimensional distribution of galaxies in the $\delta_8 - \alpha_5$ space. The black solid, red dashed and blue dotted-dashed lines show the full sample, BC1 and BC2 respectively. We find that the distributions of environmental measures are stable against these boundary effects except regions with mean δ_8 and high α_5. We then look at the LRG fraction as a function of α_5 and δ_8 for each of these samples. The left and middle panel of Figure A3 show the LRG fraction for the eBOSS sample with boundary cut of BC1 and BC2 respectively. The overall trend of the LRG fraction seems to be stable against boundary effects. Although the impact of the boundary seems to be small, we use galaxies with BC2 selection for our main results to avoid any possible influence of boundary effects.

We also note that the number density of LRGs drops sharply above redshift 0.9 due to the limits of the telescope,

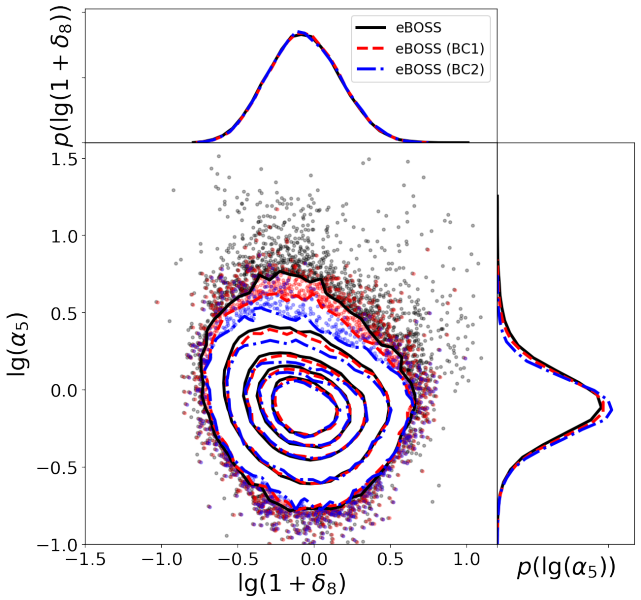

Figure A2. Comparison between the 2D distributions of the full eBOSS galaxy sample and its two sub-samples BC1 and BC2 after applying respective boundary cuts. The two sub-panels on the top and on the right show the marginalised distributions of $\log_{10}(1+\delta_8)$ and $\log_{10}(\alpha_5)$, respectively. The galaxies at the boundary are more populated at high α_5 and hence this might reflect boundary effect in our environment calculation.

which at high redshift can detect only relative luminous objects. We wanted to assess if our results are robust against such selection in the LRGs. Therefore, we created a sub-sample with boundary cut BC2 and redshift cut between 0.7 and 0.9. The right most panel in Figure A3 shows the LRG fraction for this sample. We note that the selection effect causing LRG number density to drop-sharply beyond redshift 0.9 has negligible effect in our estimate of the quenching efficiency as a function of tidal environment.

APPENDIX B: ERROR IN LRG FRACTION AND HOD MODELS

Figure B1 shows a comparison of the LRG fraction with environment between the standard HOD model and HMQ. We also show 100 times the statistical error on LRG fraction in each cell.

This paper has been typeset from a TEX/LATEX file prepared by the author.

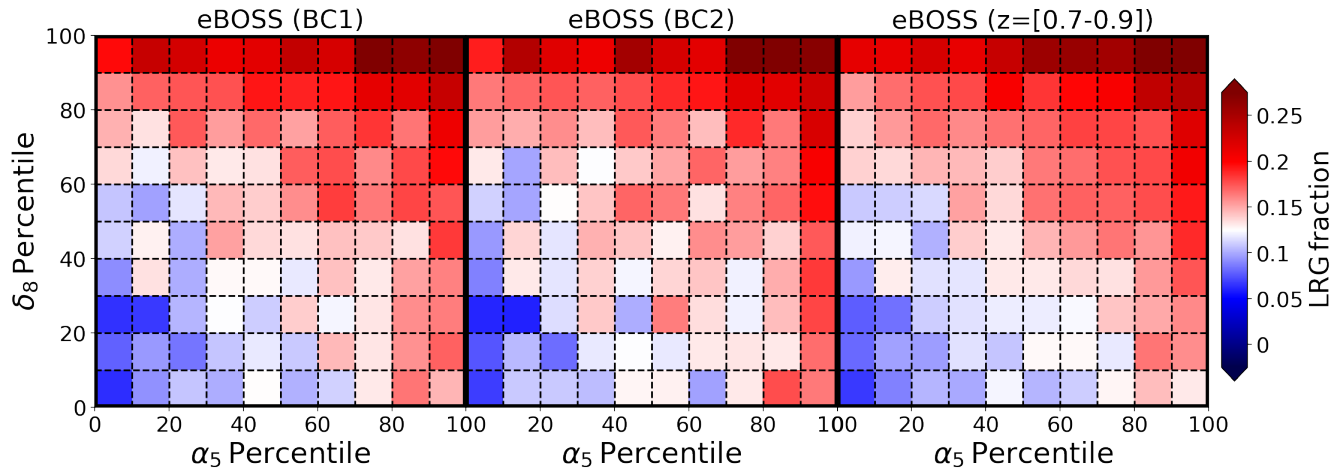

Figure A3. The same as Figure 8 but for different boundary cuts. The left, middle and right panels represent the full eBOSS sample, BC1, and BC2 respectively. The overall trend of the LRG fraction in this space is robust against boundary effects.

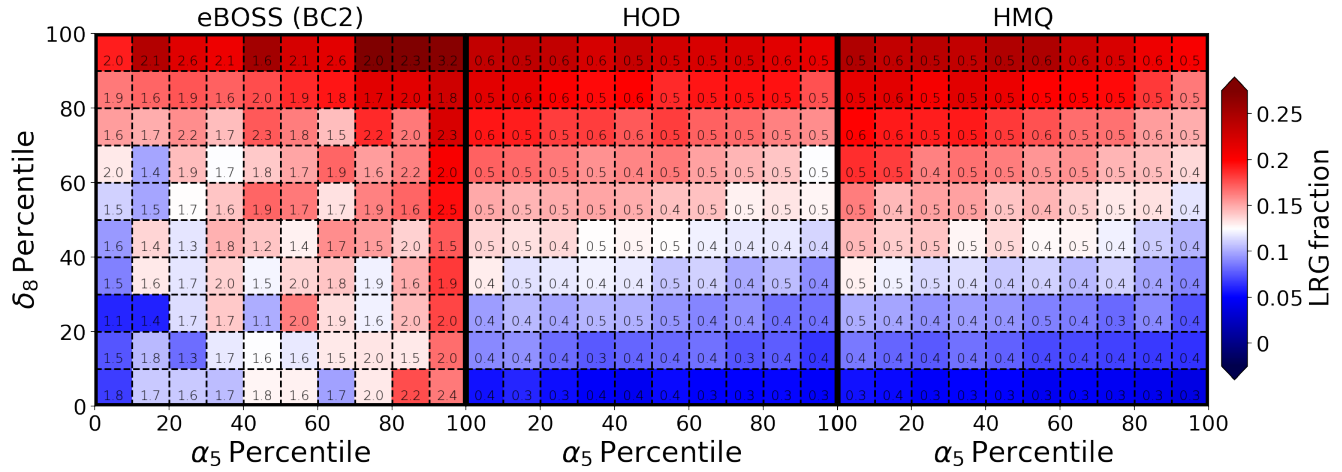

Figure B1. The same as Figure 8, but comparing eBOSS data with the normal and HMQ models including the errors. The left panel shows the eBOSS data with BC2 cuts, the middle panel is for an HOD with no halo mass quenching and the right panel is for the HMQ model. The number displayed in each cell shows 100 times the statistical errors on the LRG fraction.